

Check for updates

# Ferroelectric Quantum Dots for Retinomorphic In-Sensor Computing

Tingyu Long, Huanyu Zhou, Jaewan Ko, Hongwei Tan, Jaemin Lim, Yanfei Zhao, Daehan Kang, Eojin Yoon, Gyeong-Tak Go, Somin Kim, Seung-Woo Lee, Chan-Yul Park, Hyojun Choi, Hyeran Kim, Hyung Joong Yun, Sung Hyuk Park, Kwan Sik Park, Jeong Woo Park, Mungeun Kim, Yong Soo Cho, Ho Won Jang, Wenqiang Yang, Min Hyuk Park, Wan Ki Bae, Sebastiaan van Dijken, Joona Bang,\* and Tae-Woo Lee\*

Quantum dots (QDs) offer significant potential for neuromorphic machine vision, owing to their high absorption coefficients, and to absorption that spans the ultraviolet-to-visible range. However, their practical application faces critical challenges in achieving accurate target recognition and tracking in low-light and dynamically-changing environments. A fundamental limitation is a result of the exciton-confinement effect of QDs, which impedes efficient exciton dissociation. To overcome this problem, we synthesized ferroelectric QDs (FE-QDs) that are functionalized with thiol-terminated polyvinylidene fluoride (PVDF-SH) ligands, and empolyed them as the photo-sensitive floating gate in an organic synaptic transistor. When a polarization voltage is applied to the organic synaptic transistors, the FE-QD film generates an electric field that counteracts exciton confinement. The process substantially facilitates exciton dissociation in QDs, and regulates charge accumulation in the channel layer. Integrated with machine learning algorithms, the QD-based device achieved 100% accuracy in detecting simulated car motion in low-light environments, highlighting the potential of adaptive, dynamic sensing technologies for applications in night vision, autonomous driving, and intelligent transportation systems.

#### 1. Introduction

The interplay between visual adaptation and dynamic memory in the human vision system enables us to effectively navigate and accurately interpret visual information in constantly-changing environments. In particular, the abilities to adapt to low-light conditions and recall visual information are critical in dynamic and complex environments. In traditional machine-vision systems, sensors, memory and processing units are physically separated, and this architecture leads to a need for extensive data transmission and processing, which cause high energy consumption, time delays, and elevated hardware costs.[1,2] The recent development of energy-efficient retinomorphic optoelectronics has made steady progress through the exploration of unconventional materials, such as 2D materials, and innovations in device architectures, such

T. Long, H. Zhou, Y. Zhao, D. Kang, E. Yoon, G.-T. Go, S. Kim, S.-W. Lee, C.-Y. Park, H. Choi, S. H. Park, H. W. Jang, W. Yang, M. H. Park, T.-W. Lee Department of Materials Science and Engineering

Seoul National University Seoul 08826, Republic of Korea E-mail: twlees@snu.ac.kr

J. Ko, M. Kim, J. Bang

Department of Chemical and Biological Engineering

Korea University

Seoul 02841, Republic of Korea E-mail: joona@korea.ac.kr

**B** 

The ORCID identification number(s) for the author(s) of this article can be found under https://doi.org/10.1002/adma.202504117

© 2025 The Author(s). Advanced Materials published by Wiley-VCH GmbH. This is an open access article under the terms of the Creative Commons Attribution License, which permits use, distribution and reproduction in any medium, provided the original work is properly cited.

DOI: 10.1002/adma.202504117

H. Tan, S. van Dijken
NanoSpin, Department of Applied Physics
Aalto University School of Science
P.O. Box 15100, Aalto FI-00076, Finland
J. Lim, J. W. Park, W. K. Bae
SKKU Advanced Institute of Nanotechnology (SAINT)
Sungkyunkwan University
Suwon 16419, Republic of Korea
H. Kim, H. J. Yun
Research Center for Materials and Analysis
Korea Basic Science Institute (KBSI)
Daejeon 34133, Republic of Korea
K. S. Park, Y. S. Cho

K. S. Park, Y. S. Cho Department of Materials Science and Engineering Yonsei University Seoul 03722, Republic of Korea H. W. Jang

Advanced Institute of Convergence Technology Seoul National University Suwon 16229, Republic of Korea

ADVANCED MATERIALS

as in-sensor computing and in-memory sensing and computing systems.[3-7]

Quantum dots (QDs) provide strong potential for neuromorphic machine vision because of their broad-spectrum absorption that spans the ultraviolet-to-visible range and high absorption coefficients and are promising for photodetection in low-light environments.<sup>[8,9]</sup> These attributes have been primarily utilized for applications in photoelectric conversion and modulation<sup>[10,11]</sup> but not for dynamically regulating photocarrier behavior within QDs under low-light conditions, which is essential for achieving efficient neuromorphic machine vision. A major challenge in realizing the dynamic response of the photoelectric signal is that QDs have a strong exciton confinement effect, which leads to high exciton binding energy that hinders effective charge separation and transport within a single QD layer in neuromorphic optoelectronic devices.<sup>[12–16]</sup> The internal electric field generated by ferroelectric materials under polarization can be beneficial for exciton dissociation and charge transport.[16-23] Grafting ferroelectric polymers to QDs as ligands can be an ideal strategy to realize single ferroelectric QDs (FE-QDs) that facilitate charge separation due to ferroelectric ligands while maintaining the good light absorption by QDs. However, this approach is challenging due to the inert nature of ferroelectric polymers and solvent incompatibility between ferroelectric polymers and QDs.

Here, we provide a single material solution of FE-QDs that combines ferroelectric functionality with QD properties to address these limitations and propose their use as a retinomorphic synaptic phototransistor in artificial vision systems that combines low-light in-sensor visual adaptation and dynamic memory (LADM). Our approach overcomes the charge-confinement effect in QDs by introducing thiol-terminated polyvinylidene fluoride (PVDF-SH) as ferroelectric ligands. These ligands were synthesized using a reversible addition-fragmentation chain-transfer (RAFT) polymerization method, followed by the reduction of the xanthate end group. This approach overcomes the challenges posed by the limited availability of the vinylidene fluoride monomer and the synthesis difficulties associated with the PVDF polymer. We introduced -SH group to facilitate the formation of active sites and provide strong binding affinity for metal ions in QDs; this change increased the success rate of ligand exchange with inorganic QDs. The capping PVDF-SH ligands onto QDs significantly reduces aggregation tendencies in the film, and thus ensures uniform QD dispersion, which is not achievable by simply physically mixing PVDF with QDs. Incorporation of PVDF

W. Yang
Institute of Atomic Manufacturing
International Research Institute for Multidisciplinary and Frontiers
Beihang University
Beijing 100191, China
T.-W. Lee
Interdisciplinary Program in Bioengineering
Institute of Engineering Research
Research Institute of Advanced Materials
Soft Foundry
Seoul National University
Seoul 08826, Republic of Korea
T.-W. Lee
SN Display Co., Ltd.
Seoul 08826, Republic of Korea

with hydrophobic  $\mathrm{CF}_2$  groups into the FE-QD layer helps provide stability in moisture and air conditions. Continuous testing of the devices in an atmospheric environment demonstrated an extraordinarily long retention time of more than 25200 s, which makes the device well-suited for use in neuromorphic machine vision applications. Application of a polarization voltage to the proposed FE-QD retinomorphic device effectively promotes exciton dissociation and dynamically controls the memory state. When combined with a machine-learning algorithm, the LADM system exploits the sensor's intrinsic scotopic adaptation and dynamic memory capabilities to detect car motion with 100% accuracy under simulated low-light conditions.

#### 2. Results

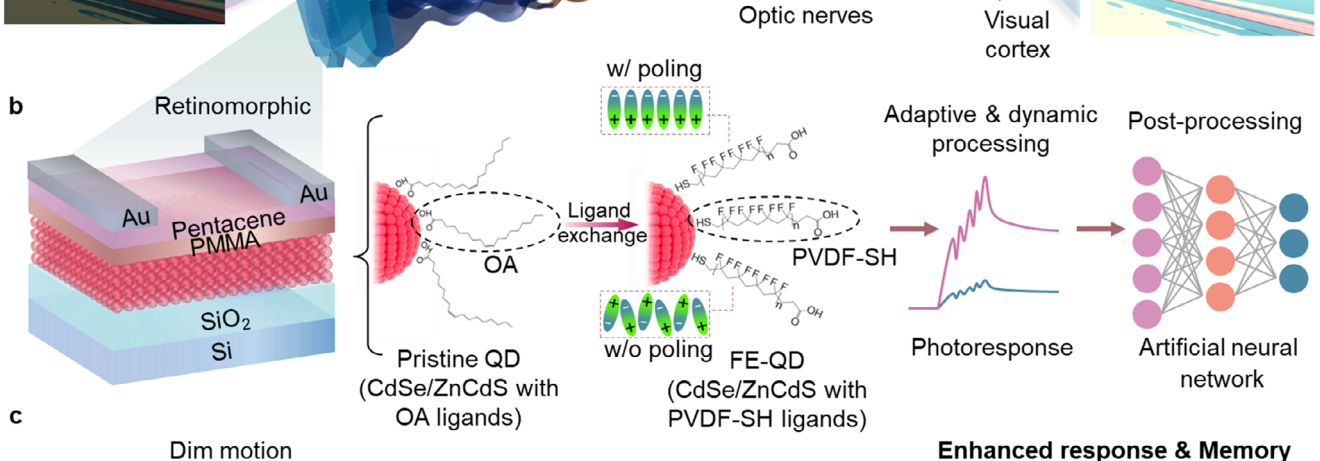
#### 2.1. Design of an Adaptive and Dynamic Memory Vision System

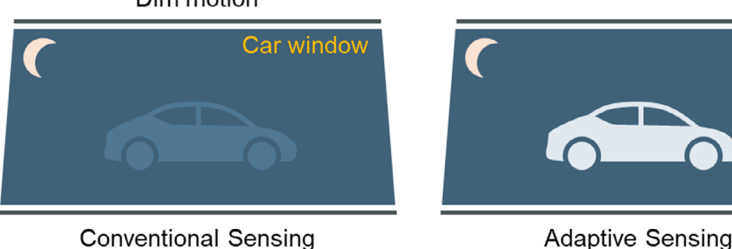
Low-light adaptive dynamic memory enhances human night vision and increases the safety of nighttime activities such as walking and driving.[24,25] It enables the vision system to quickly adapt to low-light conditions; this reduction in the time required for adjustment improves functional efficiency in new environments. [26,27] The detection and adaptation to lowlight conditions are performed by rod cells, which are highly photosensitive. [28,29] When light from an external object strikes photoreceptor cells (rods and cones) in the retina (Figure 1a), the light stimulus is converted to electrical impulses that are transmitted to the brain. In the brain, neurons transmit information through synapses, where synaptic plasticity – changes in the strengths of synaptic connections – plays a crucial role. Repeated stimulation strengthens these connections, and thereby forms visual memories. When new experiences conflict with existing memories, neuroplasticity allows for the modification or reorganization of these memories; this adaptability enables dynamic memory processes.

Inspired by the biological vision system's ability to adapt and retain dynamic memory in low-light conditions, we propose an artificial perceptual vision memory system that uses transistor structures composed of QDs modified with ferroelectric PVDF-SH ligands (Figure 1b). These synaptic phototransistors are constructed with a floating gate configuration, with a layer of CdSe/ZnCdS QDs serving as the floating gate between two gate insulators. To increase the system's capabilities for low-light detection and scotopic adaptation, oleic acid (OA) ligands on the synthesized QDs are replaced with PVDF-SH ligands, which have ferroelectric properties. When a polarization voltage  $(V_{pol})$  is applied, it aligns the dipoles of the PVDF-SH ligands; this alignment generates an internal electric field that facilitates the separation of photogenerated electron-hole pairs (EHPs) in the QDs. This accelerated separation dynamically regulates the accumulation and depletion of holes in the channel, thereby affecting the device's memory level. These FE-QDs, which combine excellent photoelectric response of QDs with the ferroelectric properties of PVDF-SH ligands, allow for dynamic adjustment of channel carrier states under  $V_{\text{pol}}$ , and thus offer substantial advantages for achieving the proposed LADM system (Figure 1c). Benefiting from the FE-QD material strategy, our unique LADM system has the potential to solve problems such as poor low-light recognition

15214095, 0, Downloaded from https://advanced.onlinelibrary.wiley.com/doi/10.1002/adma.202504117 by Seoul National University, Wiley Online Library on [04/09/2025]. See the Terms and Conditions (https://onlinelibrary.wiley.com/terms

-and-conditions) on Wiley Online Library for rules of use; OA articles are governed by the applicable Creative Commons







Adaptive & Dynamic Sensing

Figure 1. Biological and artificial vision systems with adaptive and dynamic sensing capabilities. a) The human visual system receives external stimuli through photoreceptors, including cones and rods, and continuously adapts by updating synaptic connections to form visual dynamic memory. Highly photosensitive rod cells are essential for weak light detection and scotopic adaptation. b) A floating gate configuration is used to implement the LADM system. The synthesis of FE-QDs involves a ligand exchange process, where the long-chain PVDF-SH ligands replace the short-chain OA ligands. The FE-QD's advantage is its ability to realize LADM functions within a single device, facilitated by the ferroelectric PVDF-SH ligand and the photoelectric response of QDs. c) Schematic diagram of car motion recognition under low-light conditions, using conventional sensing, adaptive sensing, and adaptive & dynamic sensing, respectively.

of car movements and inadequate dynamic trajectory storage that challenge traditional sensing and adaptive-sensing systems.

#### 2.2. Synthesis and Analysis of FE-QDs

FE-QDs were synthesized by replacing the native OA ligands with functional PVDF-SH ligands (Figure 2a). PVDF-SH was synthesized using the RAFT polymerization method (Figures S1-S4, Supporting Information). The <sup>1</sup>H nuclear magnetic resonance (NMR) spectra of PVDF-xanthate and PVDF-SH (Figures \$2 and S3, Supporting Information) revealed two broad H peaks; one corresponds to methylene units in -CF2-CH2-CH2-CF2- (headto-head), and one corresponds to-CH2-CF2-CH2-CF2- (head-totail) conformations of the repeating units of PVDF. [30] Thus, the <sup>1</sup>H NMR and UV-Vis absorption spectroscopy (Figure S4, Supporting Information) results confirmed the successful synthesis of the desired PVDF-SH ligand. The introduction of -SH facilitates the formation of active sites, [31,32] which have strong binding affinity for metal ions (Cd<sup>2+</sup>), [32,33] and thereby increases the success rate of ligand exchange with inorganic QDs. The synthesized QDs were comprised of a 2-nm CdSe core and a 6-nm ZnCdS shell, coated with either OA (pristine QDs) or PVDF-SH (FE-QDs) ligands (Figure S5, Supporting Information). The normalized photoluminescence (PL) intensity responses of the pristine QDs and FE-QDs (Figure S6, Supporting Information) showed that the wavelength of the peak remained unchanged after OA had been replaced with PVDF-SH ligands. Both types of QDs had nearly identical and highly stable PL intensity under continuous illumination for 1 h (Figure S7, Supporting Information). To assess the thermal properties of FE-QDs, thermogravimetric analysis (TGA) (Figure 2b) and differential scanning calorimetry (DSC) (Figure S8, Supporting Information) were performed. Weight loss during TGA indicated that the PVDF-SH ligand content was ≈48%, based on the final weight of FE-QDs. The grafting density  $\rho$  was calculated (details in the Method section) to be ~ 1.25 chains per nm<sup>2</sup>. Additionally, DSC results showed characteristic double endothermic peaks at 150 and 163 °C during

15214095, 0, Downloaded from https://advanced.onlinelibrary.wiley.com/doi/10.1002/adma.202504117 by Seoul National University, Wiley Online Library on [04/09/2025]. See the Terms and Conditional University of Conditional Unive

library.wiley.com/terms-and-conditions) on Wiley Online Library for rules of use; OA articles are governed by the applicable Creative Commons

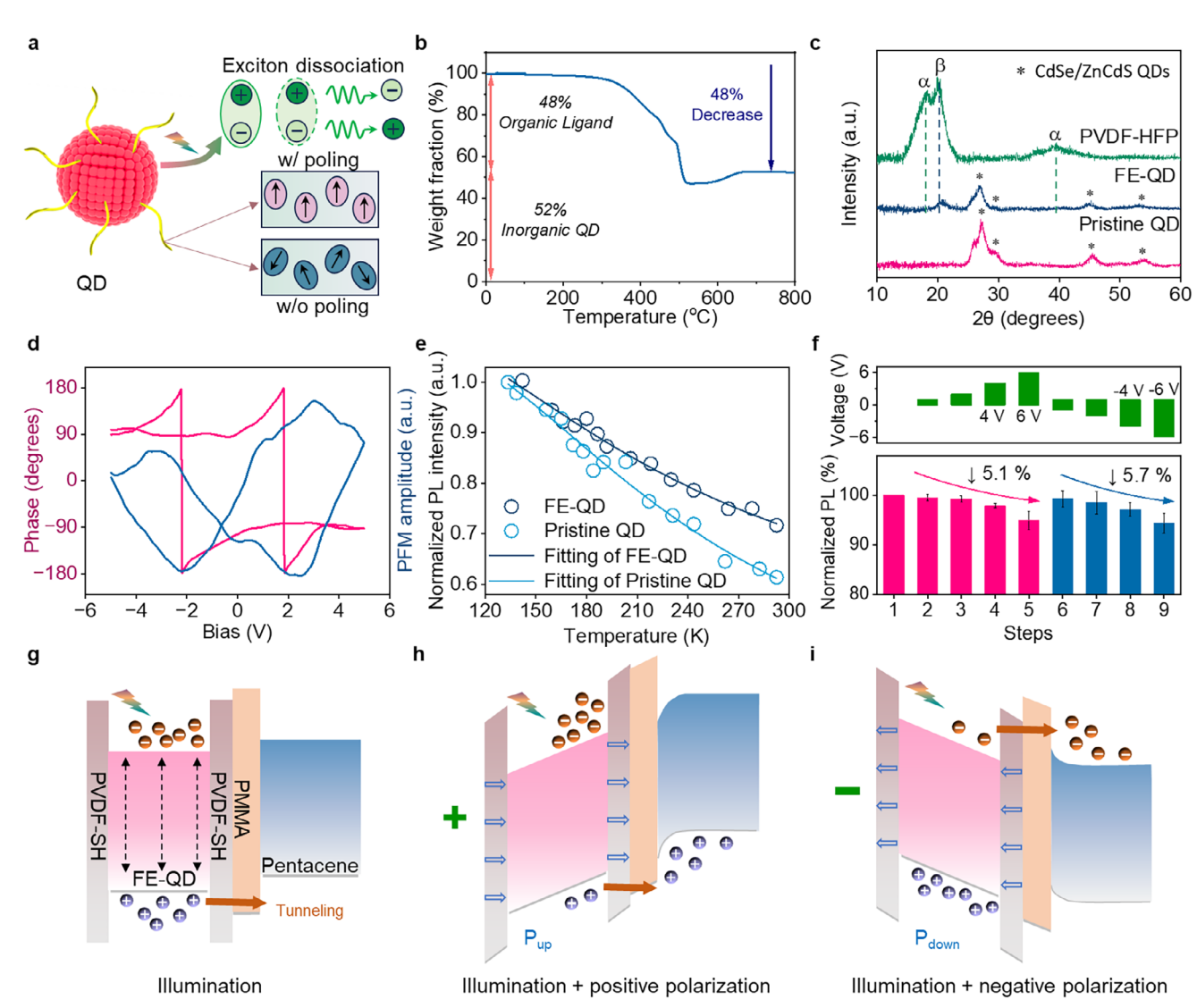


Figure 2. Synthesis and characteristics of FE-QDs. a) The presence of ferroelectric PVDF-SH ligand of FE-QD promoted exciton dissociation. b) TGA profiles of the synthesized FE-QD. c) XRD analysis comparing the crystalline structures of the PVDF-HFP film, the FE-QD film, and the pristine QD film. d) Phase hysteresis loop and amplitude hysteresis loop of the FE-QD thin film, demonstrating the ferroelectric properties. e) PL intensity as the function of temperature, derived from consistent spectral measurements. f) Average in situ PL intensity changes of 3 FE-QD samples. g) Diagrams illustrating the photogenerated carriers generation process during the light illumination. Transfer of photogenerated carriers within the device after h) positive and i) negative polarization, highlighting the impact of ferroelectric polarization on carrier dynamics.

heating, and an exothermic crystallization peak at 124 °C during cooling; these results are consistent with previous reports. [30] These findings indicate the presence of characteristic noncentrosymmetric ferroelectric PVDF crystals in the synthesized FE-QDs.

The presence of the ferroelectric phase in PVDF-SH ligands was further confirmed through X-ray diffraction (XRD) analysis(Figure 2c). The diffraction pattern of poly(vinylidene fluorideco-hexafluoropropylene) (PVDF-HFP) was used as a reference; it showed peaks at 18.3°, 20.2°, and 39.5°, which correspond to  $\alpha(020)$ ,  $\beta(110)/\beta(200)$ , and  $\alpha(002)$ , respectively, consistent with previous reports.[34,35] FE-QDs had a diffraction peak at 20.6°, which indicates the presence of the ferroelectric  $\beta(110)/\beta(200)$ phase in PVDF-SH ligands. In contrast, the pristine QDs did not show any signs of  $\alpha$  or  $\beta$  phases; this lack confirms that the ferroelectric phase originated solely from the PVDF-SH ligands. Fourier transform infrared spectroscopy (FTIR) also confirmed the presence of the  $\beta$  phase, with peaks at 510, 840, 880, 1170, 1275, and 1400 cm<sup>-1</sup>, corresponding to various stretching and rocking vibrations of CF<sub>2</sub> and CH<sub>2</sub> groups (Figure S9, Supporting Information),[34-36] with the 1275 cm<sup>-1</sup> peak appearing as a shoulder. To further confirm the ferroelectric behavior of the FE-QDs. the polarization-electric field (P-E) hysteresis loops and positiveup-negative-down (PUND) measurements were conducted for both the pristine QDs and the FE-QDs (Figure \$10, Supporting Information). The PUND measurement can evaluate true ferroelectric polarization while separating it from non-ferroelectric contributions such as dielectric response or leaky currents. The



ADVANCED MATERIALS

www.advmat.de

measurement consists of a reset pulse, followed by positive pulses (P and U) and negative pulses (N and D). The remnant polarization (P<sub>a</sub>) was calculated by subtracting the charge density of the U pulse from that of the P pulse. A similar calculation applies to the negative polarization. The FE-QDs exhibited a clear P-E hysteresis loop (Figure S10a, Supporting Information), which indicates switchable polarization. In contrast, the pristine QDs showed a nearly linear dielectric response without observable hysteresis; this result confirms their non-ferroelectric nature. Then poling time for the PUND measurement was increased to 2.5 s to increase the polarization (Figure S10b, Supporting Information). This PUND measurement provided additional evidence for intrinsic ferroelectric switching in the FE-QDs. These results collectively confirm that the ferroelectricity in the FE-QDs originates from the PVDF ligand layer, and that the core QDs themselves remain non-ferroelectric. However, compared to hybrid ferroelectric single crystals, polarization is smaller in FE-QDs; the decrease is attributed to randomly-oriented nanodomains that are caused by the presence of QDs. [37-39] The effect of poling voltage on the surface potential (Figure S11, Supporting Information) of FE-QD films was confirmed by Kelvin probe force microscopy (KPFM). When positive and negative bias voltages were applied to the surface of the FE-QD film, its surface potential changed significantly; this effect can be attributed to polarization switching and to charge injection from the conductive probe during the poling process.[40-43] Piezoresponse force microscopy (PFM) measurements produced out-of-plane phase and amplitude mapping images of the inverse piezoelectric effect (Figure S12, Supporting Information), which validated the ferroelectricity of the FE-QDs. The distribution of intensities (Figure \$12, Supporting Information, inset) is Gaussian-like at -90°; this result indicates well-aligned ferroelectric polarization along the vertical direction in the film. This observation is consistent with literature descriptions that show a uniform phase distribution in films without obvious ferroelectric polarization. [44,45] When the films were subjected to voltage changes from +5 V to -5 V, PFM detected a 180° phase lag of the phase loop and a classic butterflyshaped amplitude response (Figure 2d), which indicate spontaneous polarization and ferroelectric switching behavior; these results further confirmed the local ferroelectric properties of the film.[36] The energy level of the FE-QDs was examined using ultraviolet photoelectron spectroscopy (UPS) (Figure S13, Supporting Information), showing a secondary cut-off position shift from 17.61 eV for pristine QDs to 16.78 eV for FE-QDs. This decrease suggests a heightened built-in field on the surface, and indicates that the presence of the  $\beta$  phase induces a relatively permanent dipole moment, which effectively separates photogenerated carriers (i.e., EHPs), and thus impacting device performance. [46]

Time-resolved transient photoluminescence (TRPL) was used to evaluate the PL lifetime ( $\tau$ ) of both pristine QDs and FE-QDs (Figure S14, Supporting Information). The pristine QDs had a lifetime of  $\tau=10.11$  ns, whereas FE-QDs had a reduced lifetime of  $\tau=5.65$  ns, suggesting that the incorporation of PVDF-SH ligands facilitates exciton dissociation due to the polarization of the ferroelectric polymer PVDF. Temperature-dependent PL analysis was performed to determine the activation energy for exciton dissociation (Figure 2e; Figure S15, Supporting Information). As the temperature was increased from 130 to 293 K in 5 K increments, the PL intensity decreased exponentially (Figure 2e); this trend

indicates a shift in the balance between exciton dissociation and radiative recombination. The relationship between PL intensity and temperature was modeled using the Arrhenius equation: [47]

$$I(T) = I_0 / \left[ A \cdot \exp\left(-\frac{E_a}{k_B T}\right) + 1 \right]$$
 (1)

where  $I_0$  is the PL intensity at 0 K, A is the pre-exponential coefficient,  $E_{\rm a}$  is the activation energy of exciton dissociation (exciton binding energy), and  $k_{\rm B}=8.617\times 10^{-5}$  eV K $^{-1}$  is the Boltzmann constant. The results yielded  $E_{\rm a}$  of 45.45 meV for pristine QDs and 35.25 meV for FE-QDs. The reduced  $E_{\rm a}$  for FE-QDs implies that incorporating the ferroelectric PVDF-SH ligand decreases the energy required for exciton dissociation. We compared the exciton dissociation mechanism in QD-based devices (Table S1, Supporting Information). Our method only uses a single material to achieve the result of reducing the exciton binding energy and promoting exciton dissociation.

To examine the effect of polarization on PL properties of two types of QDs, in situ PL measurements were conducted on an ITO/QD/ITO sandwich structure with varying  $V_{pol}$  for 2 min at each stage (Figure 2f; Figure S16, Supporting Information). As the V<sub>pol</sub> increased, the PL intensity of the FE-QDs gradually decreased, and the emission red-shifted from 632 nm to 636 nm (Figure S16a–c, Supporting Information). At  $V_{\rm pol}$  at 6 V, the PL intensity decreased by 6%, but when a reverse  $V_{\rm pol}$  was applied, the PL intensity recovered to 100% of the pristine intensity, accompanied by a 4 nm blue-shift back to initial position at 632 nm. The PL intensity remained stable under illumination for 60 min without encapsulation (Figure S7, Supporting Information); this result confirms photostability and measurement reliability. Three FE-QD samples were measured, and the average results is summarized in Figure 2f. Applying a small reverse voltage (near  $\pm 2 \text{ V}$ ) to the ITO/FE-QD/ITO structure triggered a rapid polarization reversal.  $V_{\rm pol}$  = 6 V caused a 5.1% decrease in the PL intensity, and  $V_{\rm pol} = -6$  V caused a 5.7% decrease. Meanwhile, all three samples showed a concurrent red shift of 4 nm in response to a poling voltage of  $\pm 6$  V. In contrast, the PL intensity of the pristine QDs did not decrease as the magnitude of  $V_{\rm pol}$  increased (Figure S16d-f, Supporting Information); in fact, due to the defect passivation by oxygen and moisture in air, the PL intensity slightly exceeded 100%. [48,49] This comparison indicates that the observed modulation of PL intensity is attributed to the built-in electric field. The difference in responses of FE-QDs and pristine QDs is a result of responses of the ferroelectric component. When subjected to a V<sub>pol</sub>, the FE-QD's PL peak undergoes a red shift due to a built-in electric field generated by the aligned dipoles of the ferroelectric ligands PVDF-SH. This internal field perturbs the band structure of the FE-QDs by the quantum-confined Stark effect. This field leads to a spatial separation of electron and hole wavefunctions; this change reduces wavefunction overlap and recombination efficiency, and consequently causes a red shift in the PL peak.[21-23] Conversely, when an FE-QD is subjected to a reverse poling voltage, the polarization direction is switched, and this change initially induces a blue shift in the PL peak due to the reconfiguration of the internal field. However, further increasing the magnitude of reverse voltage increases the internal electric field in the opposite direction; this change also reduces the wavefunction overlap and recombination efficiency, so the PL

ADVANCED MATERIALS

www.advmat.de

peak then undergoes red shift. In contrast, pristine QDs lack ferroelectric components and therefore do not develop these built-in fields. As a result, no PL peak shift is observed under the same poling conditions as applied to the FE-QDs. These results suggest that applying  $V_{\rm pol}$  increases the polarization of surface dipoles in the FE-QD film, and thereby promotes exciton dissociation and reduces PL intensity.

With this information about the ferroelectric properties of FE-QDs after incorporation of PVDF-SH ligands, we propose the working mechanism of the LADM system (Figure 2g-i). The thicknesses of the layers of the LADM device differ (Figure \$17, Supporting Information). Under light illumination, both the FE-QDs and the pentacene rapidly generate many electronhole pairs. When the illumination is turned off, the photogenerated carriers in pentacene rapidly recombine, and do not contribute to photosynapse behavior (Section 2.3). When  $V_{pol}$  is not applied, band bending allows photogenerated holes to escape from FE-QDs into the pentacene layer, so photocurrent increases (Figure 2g). Photogenerated electrons remain in the FE-QD layer, while holes tunnel through the PMMA layer into the channel.<sup>[50]</sup> After the illumination is turned off, trapped charge carriers are retained by the potential well, and the holes in the pentacene layer require time to go back to recombine with the electrons; this delay yields long-term potentiation (LTP). The results shown in Figure 2h,i correspond to conditions where the poling voltage exceeds the coercive field. Under positive gate bias, positive polarization (Figure 2h) aligns the dipoles in the FE-QDs; this process generates an upward polarization domain, which increases hole tunneling through the PMMA layer and inhibits carrier recombination, and thereby increases long-term memory. Conversely, when negative polarization (Figure 2i) is applied, the energy band bending is rearranged oppositely. Coupled with the built-in electric field formed by negative polarization, this inverse band bending both prevents photogenerated holes from entering the channel layer and promotes trapped electrons in the FE-QD layer into the interface of the channel layer. When the illumination is turned off, the photogenerated carriers in pentacene rapidly recombine, whereas the injected electrons gradually recombine with holes in the channel layer, and thereby reduces photocurrent. Thus, positive polarization increases the photocurrent retention time, whereas negative polarization gradually decreases it. The device's response to light pulses can therefore be modulated by controlling the dipole polarization direction in the FE-QD layer, and this modulation ability can be exploited to enable various synaptic functions.

## 2.3. Optoelectronic Characteristics of FE-QD Ferroelectric Phototransistors

To demonstrate the capabilities of our LADM system for scotopic dynamic visual in-memory sensing and computing, we evaluated the optoelectronic properties of the device. The transfer curves of three types of phototransistor devices without light illumination were compared (Figure S18, Supporting Information). The transfer curves of devices with organic semiconductor (OSC)/PMMA or OSC/PMMA/pristine QD structures showed negligible hysteresis windows, whereas the device with an OSC/PMMA/FE-QD structure had a distinct hysteresis window. Little hysteresis was

observed in the double sweeping curves over a gate voltage ( $V_{\rm G}$ ) range of –5 to 5 V. However, when  $V_{\rm G}$  exceeds the coercive voltage ( $V_{\rm C}$ ) of the ferroelectric material, polarization occurs, and causes a hysteresis effect.<sup>[16]</sup> Consequently, as the  $V_{\rm G}$  range is gradually increased, the counterclockwise hysteresis loop in the double sweeping curves expands (inset of Figure S18, Supporting Information). The device's effective capacitance is  $\approx$ 0.23 nF cm $^{-2}$ . The calculated trap densities in the fabricated phototransistor were  $5.95\times10^{10}$  cm $^{-2}$  in darkness and  $2.34\times10^{10}$  cm $^{-2}$  under illumination; the difference is  $3.61\times10^{10}$  cm $^{-2}$  in light-induced trap density (details in Methods).

To demonstrate the photoelectric properties of FE-QD devices, we compared their normalized photoresponse to that of pristine QDs (Figure 3a). The synaptic phototransistor that incorporates FE-QDs showed a slower rise in current and a higher maintained synaptic weight change (13% higher at 140 s) than the device that incorporates pristine QDs. In the structure without the QD floating gate layer (Figure \$19a, Supporting Information), the PMMA layer's ability as a gate insulator to capture charges at the PMMA/OSC interface is very limited. Furthermore, the photogenerated EHPs from the pentacene layer cause only transient changes in the photocurrent, so the photocurrent remains constant during illumination. When the illumination is removed, the photocurrent immediately returns to its original state. Without a FE-QD layer, the synaptic characteristic was not observed with only the photosensitive material pentacene. Moreover, in the structure with the QD floating gate layer (Figure \$19b, Supporting Information), a thick PMMA layer (10%) significantly reduced the photoresponse retention; this result indicates the suppression of charge tunneling through the layer. Thus, the increased maintained synaptic weight change in the FE-QD synaptic phototransistor originates from the presence of polar dipoles in the ferroelectric PVDF-SH ligands.

The color-selective function of the device was evaluated using different wavelengths ( $\lambda$ ) of LED light: red ( $\lambda$  = 625 nm), green  $(\lambda = 520 \text{ nm})$ , blue  $(\lambda = 460 \text{ nm})$  and ultraviolet (UV,  $\lambda = 365$ nm). The photocurrent was measured as a function of time under illumination with a light intensity of 4  $\mu$ W cm<sup>-2</sup> (Figure 3b). EHPs were generated immediately after illumination began. The device exhibited different photonic responses when exposed to various wavelengths of LED light. When exposed to green or blue light, the device had a measurable photoresponse (Figure S20, Supporting Information), although it was not as strong as under UV illumination. Upon exposure to UV, the photocurrent response was notably different from the start compared to other wavelengths; this distinction allows the device to distinguish UV light from other colors. This excitation increases the number of free electrons and holes in the semiconductor, and a consequent increase in photocurrent.<sup>[51,52]</sup> As the power of UV light was increased from 2 nW cm $^{-2}$  to 18  $\mu$ W cm $^{-2}$ , the production of lightinduced EHPs increased, and caused a corresponding increase in the photocurrent (Figure \$21, Supporting Information).

The LADM system exhibited various synaptic characteristics under UV irradiation (Figure S19, Supporting Information). The system demonstrated paired-pulse facilitation (PPF) (inset of Figure S22a, Supporting Information), a type of short-term potentiation (STP) induced by two consecutive light pulses. A PPF index is defined as  $100\% \times A_2/A_1$ , where  $A_1$  and  $A_2$  are the excitatory postsynaptic currents (EPSC) peak intensities after applying

15214095, 0, Downloaded from https://advanced.

slibrary.wiley.com/doi/10.1002/adma.202504117 by Seoul National University, Wiley Online Library on [04/09/2025]. See the Terms and Conditions (https://onlinelibrary.wiley.com/terms

and-conditions) on Wiley Online Library for rules of use; OA articles are governed by the applicable Creative Commons

www.advancedsciencenews.com

ADVANCED MATERIALS

www.advmat.de

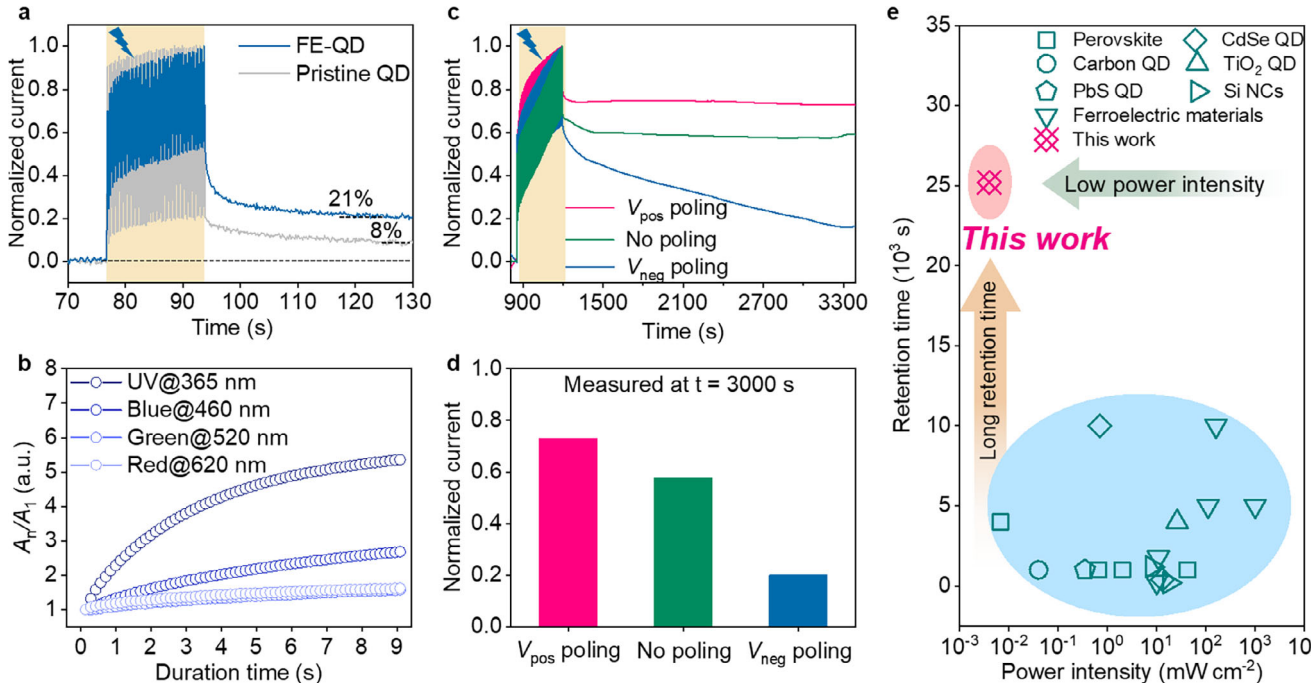


Figure 3. Photoresponses of a UV-ultrasensitive vision neuromorphic system utilizing FE-QD-based ferroelectric phototransistors. a) Photoelectric properties comparison of two types of QD-based devices subjected to 50 consecutive UV light pulses (4 μW cm<sup>-2</sup>,  $t_{\text{light}} = 20$  ms,  $\Delta t = 20$  ms,  $V_D = -0.3$  V,  $V_G = 0$  V). b) Photocurrent response as a function of time when exposed to red, green, blue, or UV light at  $V_D = -0.3$  V and  $V_G = 0$  V.  $A_n/A_1$  represents the ratio of the peak EPSC of the *n*-th optical pulse to that of the first optical pulse. c) Photocurrent variation in the LADM system under 50 consecutive light pulses (4 μW cm<sup>-2</sup>,  $t_{\text{light}} = 3.4$  s,  $\Delta t = 3.4$  s) with and without polarization applied. d) Normalized retention current levels 300 s for cases without poling, with negative poling, and with positive poling. e) Retention time of the LADM system compared to other reported systems.

the first and the second light pulses, respectively. As the interval between the light pulses was decreased, the PPF index increased to a maximum of 112% (Figure S22a, Supporting Information). The LADM also displayed spike-frequency-dependent plasticity, spike-number-dependent plasticity, and spike-duration-dependent plasticity (Figure S22b–d, Supporting Information). As spike frequency, number, and duration increased, postsynaptic currents also increased, and eventually the response changed from STP to LTP (Figure S22c,d, Supporting Information). Increasing the duration of irradiation, the frequency, or the number of light pulses increased the generation of photoinduced EHPs, which in turn increased the number of photogenerated holes entering the OSC layer, ultimately increasing the EPSC (Figure S22b–d, Supporting Information).

The ferroelectric properties of the LADM system significantly influenced its photocurrent. The system's polarization state can be switched by modulating  $V_{\rm G}$  (Figure 3c). Consequently, the polarization electric field's influence on the FE-QDs can be exploited to regulate the photoelectric properties under UV light. When the applied positive  $V_{\rm G}$  exceeds  $V_{\rm C}$ , the dipoles in the FE-QDs become positively polarized, causing more holes to accumulate in the channel. Conversely, when  $V_{\rm G}$  is negative, the dipoles reverse polarization, so the number of holes in the channel decreases. Initially, 50 UV light pulses (4  $\mu$ W cm<sup>-2</sup>) were applied to the LADM device, with the retention time maintained for >3000 s. Positive (10 V) or negative (–20 V)  $V_{\rm pol}$  was then applied to induce upward or downward polarization, respectively, then removed. After a 3-min interval, another 50 UV light pulses

(4 μW cm<sup>-2</sup>) were applied. Following positive polarization, the maintained synaptic weight change increased from 58% to 73% at 3000 s, whereas after negative polarization, the maintained synaptic weight change decreased from 58% to 20% (Figure 3d). The photocurrent response before normalization confirms that both positive and negative polarization increase the number of carriers that enter the channel, but have different effects on the decay behaviors of LTP (Figure S23, Supporting Information). Moreover, the retention current of two types of QD-based devices were also measured to a range of poling voltages from -10 V to 20 V (Figure S24, Supporting Information). Six  $V_{pol}$  (three positive, two negative, one 'zero' state) were applied to the gate electrode, then after a wait of 1 min, the device was illuminated for 30 s. The device that used FE-QDs developed a distinct photoresponsivity states for each  $V_{pol}$ , whereas the device that used pristine QDs did not show any significant change in current. The results indicate that the retention current increased with increasing positive polarization voltage, but decreased with enhanced negative polarization. This demonstrates that ferroelectric polarization enables modulation of channel carriers in the device.

The photosynapses developed in this study offer the advantage of low energy consumption because they simultaneously implement the functions of a photoelectric signal detector and artificial synapse in a single device, and thus eliminate the need for separate sensing elements that consume additional energy.<sup>[53]</sup> When the LADM system was exposed to 50 consecutive light pulses, each lasting 3.3 s, the photocurrent signal changed permanently, and the photocurrent retention time extended to >7 h (Figure



age contrast over time mimics the retina's scotopic adaptation, in which the eye takes time to adapt in dim environments and discern the surrounding clearly. One minute after the  $V_{\rm pol}$  and UV illumination were removed (Figure S29, Supporting Information), the signal 'H' under weak light can still be clearly identified. These results demonstrate that the adaptive strategy within this bionic sensor extends the control of device conductance using different polarities of materials, and thereby enhances the image perception. This simplification of hardware and algorithms increases the sensing terminal's image processing capabilities.

S25, Supporting Information). This LTP result was obtained in ambient atmospheric conditions; this result demonstrates the device's excellent stability. This good stability results from the PVDF-SH ligand, which has good oxidative and chemical stability due to the -CF<sub>2</sub> groups on PVDF.<sup>[54]</sup> This important improvement ensures the material's reliability and operation lifetime under atmospheric environmental conditions. We continuously tested the devices in an atmospheric environment and obtained the extraordinarily long retention time more than 25200 s among artificial photosynapses using photosensitive nanomaterials or ferroelectric materials (Figure 3e; Table S2, Supporting Information).

tance characteristics were exploited to achieve recognition by a three-layer artificial neural network (ANN). The ANN consisted of 784 input neurons, 100 hidden neurons, and 10 output neurons, and was used to classify images of handwritten digits in 28 × 28 pixel images (Figure S26a, Supporting Information). The conductance of the LADM system represents the synaptic weights in the ANN. Simultaneous application of positive polarization and UV illumination increased the synaptic weight. After the illumination was removed, application of negative polarization reduced the synaptic weight. Tests involved applying 30 consecutive polarizing voltage spikes for a write operation, followed by 30 suppression spikes for an erase operation (Figure S26b, Supporting Information). The results of 20 write-erase cycles (Figure \$27a,b, Supporting Information) demonstrated low cycle-to-cycle variation in operations that used  $>10^3$  polarization pulses. These reproducible conductance changes and low cycleto-cycle variation confirm the low process noise and reliability of multiple conductance states in the LADM system. The ANN was trained using the LADM cross arrays to classify the Modified National Institute of Standards and Technology (MNIST) dataset. After 40 training epochs, the ANN achieved a training accuracy of 92.2%, which is comparable to the ideal value (98.2%) (Figure \$28, Supporting Information). These results demonstrate that our strategy for developing artificial vision systems with the capabilities of LADM makes them viable candidates for neuromorphic computing applications.

By exploiting the LADM system's capability to detect weak light and modulate conductance via  $V_{\mathrm{pol}}$  control, the LADM array can simulate the dynamic sensing and adaptation functions (scotopic adaptation) and computing processes of the human retina. A  $3 \times 3$  device array was used to detect objects under low-light illumination. Two signals were applied simultaneously: a desired signal 'H' at  $\lambda = 365$  nm and a noise signal 'T' at  $\lambda = 620$  nm (Figure 4a). Scotopic adaptation gradually identified the desired signal 'H'. The current of the 9-pixel array changed over time, and exhibited different behaviors depending on whether or not  $V_{\rm pol}$  was applied (Figure 4b). Polarization significantly increased the detection sensitivity. The detection of the 'H' pattern over time under low-light was assessed by the photocurrent generated with or without polarizing voltage pulses. When  $V_{\rm pol}$  was applied, the 'H' signal became increasingly distinct as the number of light pulses increased (Figure 4c). This increase in im-

2.4. Scotopic Adaptation for Low-Light Image Recognition

To further illustrate the sensor's scotopic adaptation for dim image recognition, we compared the classification accuracies of a dim MNIST dataset using a simulated sensor array, either subjected to  $V_{\text{pol}}$  (scotopic adaptation) or not (no adaptation). The simulation assumed a pre-trained convolutional neural network (CNN) model (Figure 4d) (details in Methods). The dim MNIST dataset was generated by scaling the amplitude by factors of 0, 0.187, 0.295, 0.625, and 1 for the scotopic adaptation sensor, and 0, 0.073, 0.082, 0.098, and 0.109 for the no adaptation sensor. The scotopic adaptation and no adaptation sensor system data were extracted from Figure 4c (detailed results in Figure \$30, Supporting Information). These five values represent the ratio of sensor amplitude when receiving 0, 5, 10, 20, and 30 optical spikes. 30% Gaussian noise was added to increase the robustness of the model. All of the above factors for dim images generation and the standard deviations for Gaussian noise generation were calculated from experimental data (Figure 4c). With scotopic adaptation, the detected image of dim '9' in the MNIST dataset became increasingly clear as the number of optical spikes increased from 0 to 30, whereas without adaptation, the image remained unclear even after 30 optical spikes (Figure 4e). Subsequently, the pre-trained CNN model was used to classify the simulated dim MNIST images with and without scotopic adaptation. With scotopic adaptation, the classification accuracy improved from an initial 10% to 95.4% after 30 spikes, compared to a maximum of ≈22% without adaptation (Figure 4f,g). Confusion matrices for the test accuracy on MNIST datasets for scotopic adaptation and no adaptation sensors (Figure S31, Supporting Information) illustrate the potential of the proposed scotopic adaptive sensor for recognizing dim images.

## 2.5. Motion-Detection Capabilities of Different Sensing Technologies in a Dim Environment

A biological vision system can efficiently process dynamic visual information due to system's short-term memory effect. Here, we combined in-sensor scotopic adaptation with the dynamic memory effect to explore potential application in motion recognition in low-light environments. This ability is crucial for autonomous night-driving technology. To demonstrate the potential application for motion recognition at night, the performance of three sensing technologies (Conventional, Adaptive, and Adaptive & Dynamic sensors) is discussed in Figure 5. We proposed four traffic situations for a car in a dim (nighttime) environment: moving away, approaching, moving left, and moving right (Figure 5a). Figure 5b, which was simulated based on the scenarios depicted in Figure 5a, was employed to train

15214095, 0, Downloaded from https://advanced.onlinelibrary.wiley.com/doi/10.1002/adma.202504117 by Seoul National University, Wiley Online Library on [04/09/2025]. See the Terms and Conditions (https://onlinelibrary.wiley.com/terms

and-conditions) on Wiley Online Library for rules of use; OA articles are governed by the applicable Creative Commons

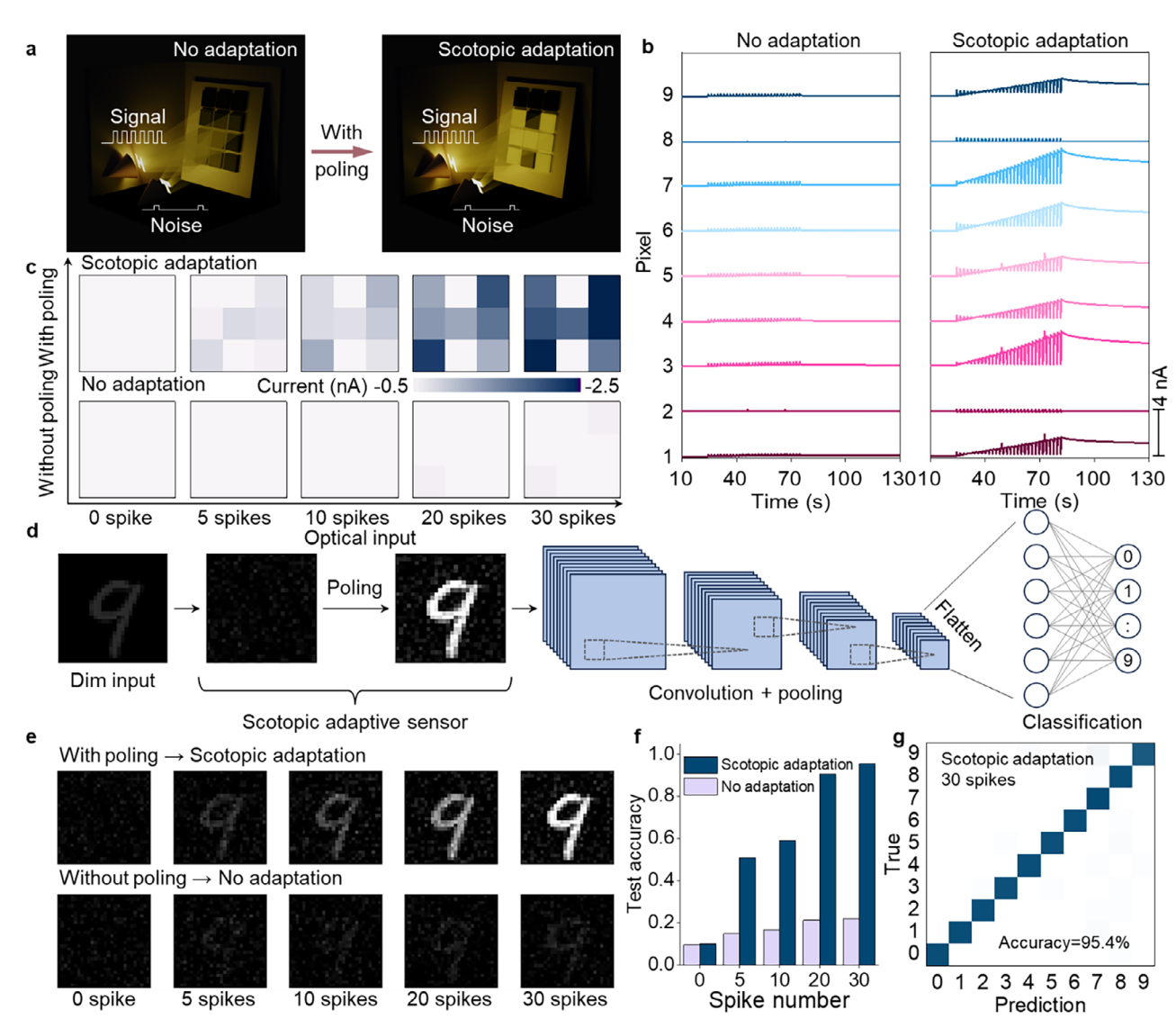


Figure 4. LADM phototransistor array for simulation of hand-written digit recognition and scotopic adaptation. a) Conceptual design of the LADM light-sensing array in a dark environment, showing the projection of a T-shaped noise light signal and an H-shaped target light signal onto the LADM array, resulting in a corresponding light-sensing image. b) Photocurrent responses of the nine pixels in the LADM array during simultaneous exposure to the noisy T-shaped signal and the target H-shaped signal, observed without ferroelectric stimuli (left) and with ferroelectric stimuli (right). c) Schematic representation of the ferroelectric effect enabling the detection of the H-shaped signal with scotopic adaptation. Comparison between the clear Hshaped signal obtained with scotopic adaptation (upper panel) and the unclear signal without adaptation (lower panel). d) Implementation of the scotopic adaptive sensor using a CNN training model for recognizing dim images. e) Simulated sensor data comparing the effects of poling for scotopic adaptation versus the condition without adaptation. f) Accuracy comparison for scotopic adaptation scenarios, both without poling and with poling. g) Confusion matrix depicting the accuracy of recognition for scotopic adaptation conditions.

our models. Conventional sensors (ConS) struggle to detect and recognize a car in dim conditions. To enhance these capabilities, a bioinspired scotopic adaptive sensor (AdaS) can detect and recognize objects in such environments, but has difficulties detecting and recognizing motion. Our adaptive and dynamic sensor (A&DS) excels in both detecting dim images and recognizing motion under these conditions. The A&DS's inherent memory allows it to store previous car positions in shortterm memory and compare these positions to detect motion. To recognize the dynamic motion in a dim environment, a CNN was trained to recognize the car motion direction by using data obtained using ConS, AdaS, or A&DS (details in Methods). Gaussian noise was added to generate 1000 datasets (800 for training, 100 for validating, 100 for testing) for each sensor type. The confusion matrices (Figure \$32, Supporting Information) showed recognition accuracy results for the four motion types under dim conditions. The A&DS achieved 100% accuracy in both training and testing (Figure 5c,d); these results far surpass the results obtained using AdaS (71%) and ConS (61%). Thus, the A&DS shows promise for applications in autonomous driving, night vision, and intelligent transport technologies.

15214095, 0, Downloaded from https://advanced.onlinelibrary.wiley.com/doi/10.1002/adma.202504117 by Seoul National University, Wiley Online Library on [04/09/2025]. See the Terms and Conditions (https://onlinelibrary.wiley.com/terms

-and-conditions) on Wiley Online Library for rules of use; OA articles are governed by the applicable Creative Commons License



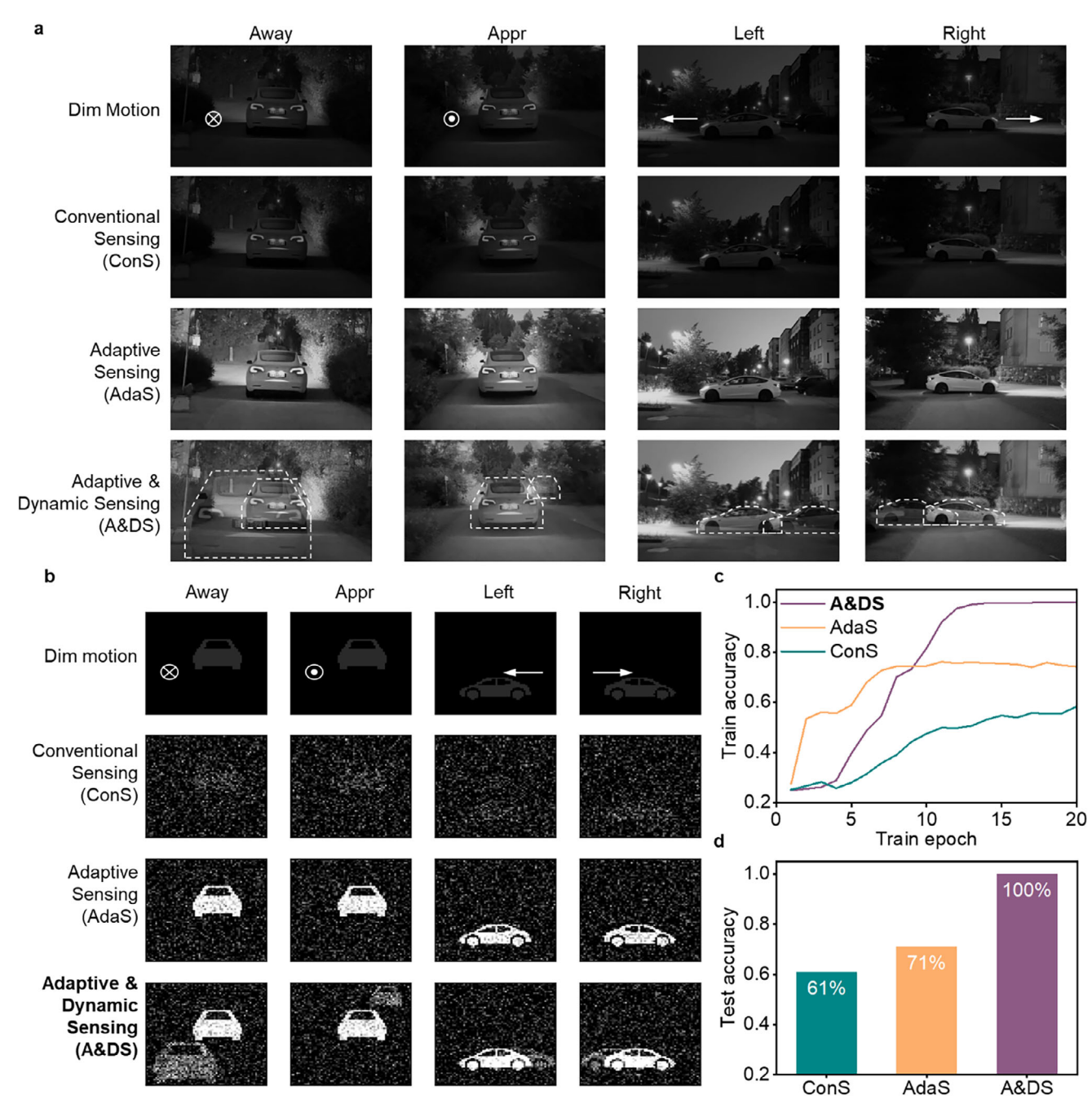


Figure 5. Motion detection abilities of different sensing technologies in dim environments. a) Original images depicting car motions in four directions in a dim environment, accompanied by the respective outputs from conventional sensors, adaptive sensors, and adaptive & dynamic sensors under dark conditions. b) Simulation results illustrating the car motion recognition abilities using three different sensor technologies - conventional, adaptive, and adaptive & dynamic - compared to the original image in a. c) Training accuracies with dim motion data acquired from conventional, adaptive, adaptive & dynamic sensors. d) Test accuracies evaluating dim motion data from the same sensor types.

#### 3. Conclusion

In this work, we synthesized FE-QDs modified with PVDF-SH ligands and applied them to develop a retinomorphic phototransistor for neuromorphic machine vision that mimics the adaptive and dynamic capabilities of biological vision systems. This innovative approach of synthesizing PVDF-SH by living free radical polymerization, then using it as ligands for inorganic QDs, is proposed for the first time in this field. By incorporating ferroelectric properties into QDs, we reduced the exciton binding energy, and thus facilitated efficient exciton dissociation. Our device that uses FE-QDs showed modulation of photocarriers in QDs with a function of gate voltage. Our device demonstrates highly tunable, non-volatile (>25200 s in atmosphere condition),



www.advmat.de

and programmable synaptic states. By integrating ferroelectricity, optical responsiveness, and low-power operation, our device enables adaptive signal amplification and enhanced recognition resolution under low-light conditions, while simultaneously supporting scotopic adaptation and dynamic memory, a critical innovation for low-light detection and in-sensor computing. With these capabilities, our device achieved 100% accuracy in detecting car motion under dim conditions, so it can contribute to significantly advanced technologies for safety-critical applications such as autonomous driving and night vision. The integration of ferroelectric materials and quantum dots into a single architecture represents a substantial step forward in the development of biomimetic vision systems, offering new possibilities for neuromorphic devices and intelligent sensing technologies. Our work highlights the potential of combining advanced materials engineering with biomimetic system design to address challenges in adaptive and dynamic sensing. This approach opens up broad possibilities for next-generation vision systems with applications in autonomous driving, security, and smart mobility.

#### 4. Experimental Section

CTA Synthesis: A solution of bromoacetic acid (3.00 g, 21.59 mmol, 1 equiv.) in 50 mL of acetone was slowly added to a mixture of potassium ethyl xanthogenate (3.46 g, 21.59 mmol, 1 equiv.) and triethylamine (2.62 g, 25.91 mmol, 1.2 equiv.) dissolved in 100 mL of acetone. The reaction was allowed to proceed overnight. After the reaction was complete, the solvent was removed using a rotary evaporator, then an equivalent amount of dichloromethane was added. Purification was performed by washing the product three times with distilled water. After drying over sodium sulfate, the solvent was removed *in vacuo*. These processes yielded 3.19 g (82% yield) of an off-white solid, identified as 2-((ethoxycarbonothioyl)thio) propanoic acid (as a CTA).  $^1$ H NMR (500 MHz, CDCl<sub>3</sub>,  $\delta$ ): 1.43 (t, J = 7.1 Hz, 3H), 3.98 (s, 2H), 4.67 (q, J = 7.1 Hz, 2H).

PVDF-SH Synthesis: RAFT polymerization was performed in an autoclave system (Series 4520 Bench Top Reactor 1 L, Parr Instruments, USA). A solution containing CTA (1.29 g, 7.14 mmol) and di-tert butyl peroxide (0.10 g, 0.71 mmol) in 500 mL of dimethyl carbonate was introduced into the reaction vessel. The autoclave was purged with Ar for 30 min, then VDF monomer gas (50 g, 780.88 mmol) was injected, and the temperature was raised to 120 °C while the pressure was raised to ≈20 bar. The solution was stirred vigorously overnight. After cooling and depressurizing the vessel to room temperature and ambient pressure (≈1 bar), and the resulting PVDF-Xanthate was precipitated into cold methanol and dried in vacuo. The polymer's molecular weight was determined by NMR, yielding  $\rm M_{n,calc} = 5500~g~mol^{-1}$  . To convert PVDF-Xanthate to PVDF-SH, the terminal xanthate group was cleaved using NaN3. Four molar equivalents of NaN3 with respect to PVDF-Xanthate were dissolved in an appropriate amount of DMF under an Ar atmosphere. Upon completion of the reaction, PVDF-SH was isolated by precipitation into cold methanol.

CdSe/ZnCdS QD Synthesis and PVDF Ligand Exchange: CdSe/ZnCdS QDs were synthesized using a previously reported method with minor modifications,  $^{[55]}$  utilizing the Schlenk line technique under inert conditions. Stock solutions of cadmium oleate (Cd(OA)2, 0.5 M), zinc oleate (Zn(OA)2, 0.5 M), tri-n-octylphosphine selenide (TOPSe, 2 M), and trin-octylphosphine sulfide (TOPS, 2 M) were prepared. A mixture of CdO (1 mmol), myristic acid (MA, 3 mmol), and octadecene (ODE, 15 mL) was degassed at 110 °C for 2 h, then heated to 270 °C to yield a clear solution. Rapid injection of 0.25 mL of TOPSe solution initiated the formation of CdSe cores. After 3-min reaction at 300 °C, 4 mL of Zn(OA)2 (0.5 M) was injected, followed by the dropwise addition of 1.5 mmol dodecanethiol (DDT) within 1 minute to grow the ZnCdS shell. After 30 minutes, successive injections of Cd(OA)2, Zn(OA)2, and TOPS were conducted to en-

hance the growth of the ZnCdS shell. The synthesized QDs were purified by repeated precipitation and redispersion technique (more than five times).

For ligand exchange, 0.5 mL of CdSe/ZnCdS QDs dissolved in toluene (100 mg mL $^{-1}$ ) was added to 4.5 mL of DMF containing 10 mg of 3-mercaptopropionic acid. After 6 h of stirring, the solution cleared. Then 75 mg of PVDF-SH was introduced, and the ligand exchange was allowed to proceed overnight. The final product, FE-QD, was obtained by precipitation in methanol, then redispersed in DMF ( $\approx\!20$  mg mL $^{-1}$ ). The grafting density ( $\rho$ ) of PVDF ligands on the QD surface was estimated from TGA data. The total chain number of PVDF ligands ( $N_{PVDF}$ ) and the total QD surface area ( $S_{OD}$ ) were calculated using the following equations:

$$N_{PVDF} = N_A \times \frac{w_{PVDF}}{MW_{PVDF}} \tag{2}$$

and

$$S_{QD} = 4\pi R^2 \times \frac{w_{QD}}{w_{singleQD}} \tag{3}$$

where  $N_{\rm A}$  is the Avogadro number,  $w_{PVDF}$  is the weight of PVDF ligands (i.e., of the organic fraction) measured using TGA,  $MW_{PVDF}$  is the molecular weight of PVDF ligands, R is the radius of a QD,  $w_{QD}$  is the weight of QD (i.e., the inorganic fraction) measured by TGA, and  $w_{singleQD}$  is the weight of a single QD. The grafting density (chains/nm²) was calculated as:

$$\rho = \frac{N_{PVDF}}{S_{QD}} \tag{4}$$

Photonic Synaptic Device Fabrication: A heavily-doped p-type silicon wafer served as both the substrate and gate electrode. The ferroelectric material FE-QD was dissolved in dimethylformamide (DMF) to form a 10 mg/mL suspension. This solution was spin-coated at 2000 rpm for 60 s (resulting in a thickness of 65 nm) on a commercial silicon substrate covered by a SiO<sub>2</sub> layer to form the first gate insulator (GI 1), then dried in a transition chamber to form the ferroelectric and photoelectric-responsive interface layer. The second gate insulator (GI 2), was formed by spincoating a poly(methyl methacrylate) (PMMA) (2 wt.% in anisole, Mw = 120 000 g mol<sup>-1</sup>, Sigma-Aldrich Korea) at 3000 rpm for 60 s, yielding a 10nm-thick film. Then pentacene was thermally evaporated onto the PMMA layer to form the OSC layer. The evaporation was conducted at a rate of 1 Å s<sup>-1</sup> under a vacuum pressure of  $3 \times 10^{-6}$  Torr, and yielded a 40-nmthick OSC layer. A 40-nm-thick Au layer was then deposited as source/drain electrodes at a rate of 1.0 Å s<sup>-1</sup> under the same vacuum conditions. The device had a channel width of 1.5 mm and a channel length of 50 µm.

Characterization: Electron micrographs were obtained using a JEM-F200 field emission transmission electron microscope (JEOL Co. Ltd., Japan), operated at 200 kV, with carbon-coated copper grids (LC300 -Cu, Electron Microscopy Sciences). X-ray diffraction (XRD) patterns were recorded using a multifunctional X-ray diffractometer (X'pert powder diffractometer, PANalytical) with Cu K $\alpha$  radiation in the range  $10 \le 2\theta \le$ 60°. Fourier transform infrared (FT-IR) spectra were obtained using a VER-TEX 80 V vacuum spectrometer (Bruker, Germany), with samples in KBr pellets. Steady-state PL spectrum and photostability were measured using a spectrofluorometer (FP-8500, JASCO) with a 405-nm excitation wavelength from a xenon arc lamp (150 W). Temperature-dependent PL was measured using a closed-cycle helium cryostat (CS-204, ARS) connected to a compressor (4HW, ARS). Excitation was provided by a picosecond pulsed laser (LDH-P-C-405B, PicoQuant GmBH) at 405 nm, pulse width < 50 ps, and repetition rate of 4 MHz, driven by a PLD 800-B driver (PicoQuant). Emitted photons were detected using a photon counting detector (PMA Hybrid 07), time-correlated single-photon counting (TCSPC) module (PicoHarp, PicoQuant), and a microchannel plate photomultiplier tube (MCP-PMT, R3809U-59, Hamamatsu). This in-situ PL measurement was conducted under constant conditions, with a fixed excitation spot position throughout the experiment. Device electrical characterization was performed using a semiconductor parameter analyzer (B1500A, Keysight)

ADVANCED MATERIALS

www.advmat.de

under ambient conditions. Atomic force microscopy (AFM) images were obtained using an NX-10 (Park system) at the Research Institute of Advanced Materials, with ferroelectric switching properties of FE-QD films assessed in PFM mode. The surface potential of the film was obtained by Kelvin probe force microscopy (KPFM, Nanoscope V multimode, Bruker, USA) and UV-Vis absorption spectra of the film was measured by UV-Vis spectrophotometer (Cary 5000, Agilent Technologies). The P-E characteristics measurement was performed using a 500 Hz triangular waveform with the TF3000 system from aixACCT. The PUND measurement was performed using a 0.2-Hz rectangular waveform with a semiconductor parameter analyzer (4200A-SCS, Keithley). The capacitance of the Si/SiO<sub>2</sub>/FE-QD/PMMA/Pentacene/Au structure device was measured at frequency range from 20 Hz to 0.1 MHz using a precise LCR meter (Agilent Keysight Technologies, E4980A). TGA analysis was conducted using a TGA Q50 instrument (TA Instruments), heating samples from 0 to 800 °C at 10 °C/min in N<sub>2</sub> atmosphere. DSC was performed using a DSC 200 F3 Maia setup (Netzsch), with samples heated from -50 to 200 °C and cooled back to -50 °C at 10 °C/min under a N2 atmosphere. Ultraviolet photoelectron spectroscopy (UPS) was conducted using an AXIS Ultra DLD (Kratos Inc.), employing a helium-gas discharge lamp with an excitation energy of 21.22 eV and an energy resolution of 200 meV within a sampling area of 100-um diameter. To minimize static electricity accumulation during the measurement process, a bias of 15 V was applied to the sample. The trap density N was calculated:[56]

$$N = \frac{C_i}{q} \left( \frac{S \log e}{kT/q} - 1 \right) \tag{5}$$

where  $C_i$ , q, S, k, and T correspond to the gate capacitance per unit area, electron charge, subthreshold swing, Boltzmann constant, and absolute temperature, respectively.

ANN Array Simulation: ANN simulations were conducted using "Cross Sim" software developed by Sandia National Laboratories, USA. The network architecture consisted of three layers with dimensions  $784 \times 300 \times 10$ . For training, 60 000 example images from the MNIST dataset were used, and for testing, 10 000 images were used.

CNN for Dim MNIST Recognition: The CNN used for recognition of dim image in MNIST (Figure 4), consisted of four Conv2D layers and four MaxPooling2D layers to extract relevant features. The classification was performed using a fully connected layer. To model was trained using 48000 images and validated using an additional 12 000 images from the MNIST dataset. After 50 training epochs, the model achieved an accuracy of 98%.

CNN for Dim Motion Recognition: For dim motion recognition (Figure 5), the CNN architecture included four Conv2D layers and four MaxPooling2D layers for feature extraction. A fully connected layer was used for classification. The CNN was trained on three different datasets: conventional sensor data, adaptive sensor data, and adaptive & dynamic sensor data; 800 datasets were used for training, 100 datasets for validation, and 100 datasets with added Gaussian noise were used for testing.

### **Supporting Information**

Supporting Information is available from the Wiley Online Library or from the author.

#### **Acknowledgements**

This work was supported by the National Research Foundation of Korea (NRF) grants funded by Ministry of Science and ICT (MSIT). (grant numbers: RS-2024-00416938 and RS-2021-NR059149).

#### **Conflict of Interest**

The authors declare no conflict of interest.

#### **Author Contributions**

T.L., H.Z., J.K., and H.T. contributed equally to this work. T.L., H.Z., J.B. and T.-W.L. conceived the idea. J.K., J.W.P., M.K. and J.L. synthesized the materials. T.L. and J.K. characterized the materials. T.L., H.Z. and W.Y. designed the experiments. T.L. fabricated the devices, performed electrical and optoelectronic measurements. T.L., D.K., H.C., E.Y., H.K., H.J.Y., C.-Y.P., S.H.P, and K.S.P., performed electrical characterization. H.T., T.L. and G.-T.G. did the simulations. H.T. wrote the code of the machine learning algorithms. T.L., H.T., J.K., H.Z., Y.Z., S.K., S.-W.L., S.v.D., J.B. and T.-W.L. cowrote the paper and all authors reviewed it. J.B. and T.-W.L. supervised the project.

#### **Data Availability Statement**

The data that support the findings of this study are available from the corresponding author upon reasonable request.

#### **Keywords**

dynamic vision perception, ferroelectric ligand, ferroelectric-controlled photoresponse, molecular design, quantum dot, scotopic adaptation

Received: February 28, 2025 Revised: July 22, 2025 Published online:

- [1] F. Zhou, Y. Chai, Nat. Electron. 2020, 3, 664.
- [2] F. Liao, Z. Zhou, B. J. Kim, J. Chen, J. Wang, T. Wan, Y. Zhou, A. T. Hoang, C. Wang, J. Kang, J.-H. Ahn, Y. Chai, Nat. Electron. 2022, 5, 84.
- [3] H. Tan, S. van Dijken, Nat. Commun. 2023, 14, 2169; M.-J. Sung, K.-N. Kim, C. Kim, H.-H. Lee, S.-W. Lee, S. Kim, D.-G. Seo, H. Zhou, T.-W. Lee, Chem. Rev. 2025, 125, 2625.
- [4] Z. Zhou, J. Fu, Z. Chen, F. Zhuge, Y. Wang, J. Yan, S. Ma, L. Xu, H. Yuan, M. Chan, X. Miao, Y. He, Y. Chai, Nat. Electron. 2023, 6, 870.
- [5] L. Mennel, J. Symonowicz, S. Wachter, D. K. Polyushkin, A. J. Molina-Mendoza, T. Mueller, *Nature* 2020, 579, 62.
- [6] A. Dodda, D. Jayachandran, A. Pannone, N. Trainor, S. P. Stepanoff, M. A. Steves, S. S. Radhakrishnan, S. Bachu, C. W. Ordonez, J. R. Shallenberger, J. M. Redwing, K. L. Knappenberger, D. E. Wolfe, S. Das, Nat. Mater. 2022, 21, 1379.
- [7] H. Jang, H. Hinton, W.-B. Jung, M.-H. Lee, C. Kim, M. Park, S.-K. Lee, S. Park, D. Ham, *Nat. Electron.* **2022**, *5*, 519.
- [8] Y. Zhang, G. Wu, F. Liu, C. Ding, Z. Zou, Q. Shen, Chem. Soc. Rev. 2020, 49, 49.
- [9] J. Du, R. Singh, I. Fedin, A. S. Fuhr, V. I. Klimov, Nat. Energy 2020, 5, 409
- [10] B. Pradhan, S. Das, J. Li, F. Chowdhury, J. Cherusseri, D. Pandey, D. Dev, A. Krishnaprasad, E. Barrios, A. Towers, A. Gesquiere, L. Tetard, T. Roy, J. Thomas, *Sci. Adv.* 2020, 6, aay5225.
- [11] H. Seung, C. Choi, D. C. Kim, J. S. Kim, J. H. Kim, J. Kim, S. I. Park, J. A. Lim, J. Yang, M. K. Choi, T. Hyeon, D.-H. Kim, Sci. Adv. 2022, 8, aba3101.
- [12] W. Yang, S.-H. Jo, Y. Tang, J. Park, S. G. Ji, S. H. Cho, Y. Hong, D.-H. Kim, J. Park, E. Yoon, H. Zhou, S.-J. Woo, H. Kim, H. J. Yun, Y. S. Lee, J. Y. Kim, B. Hu, T.-W. Lee, Adv. Mater. 2023, 35, 2304533.
- [13] A. Miyata, A. Mitioglu, P. Plochocka, O. Portugall, J. T.-W. Wang, S. D. Stranks, H. J. Snaith, R. J. Nicholas, Nat. Phys. 2015, 11, 582.
- [14] S. Zhang, R. Chen, D. Kong, Y. Chen, W. Liu, D. Jiang, W. Zhao, C. Chang, Y. Yang, Y. Liu, D. Wei, Nat. Nanotechnol. 2024, 19, 1323.





www.advmat.de

- [15] C. Wang, Y. Bian, K. Liu, M. Qin, F. Zhang, M. Zhu, W. Shi, M. Shao, S. Shang, J. Hong, Z. Zhu, Z. Zhao, Y. Liu, Y. Guo, *Nat. Commun.* 2024, 15, 3123.
- [16] R. Yu, L. He, C. Gao, X. Zhang, E. Li, T. Guo, W. Li, H. Chen, Nat. Commun. 2022, 13, 7019.
- [17] M. K. Kim, J. S. Lee, Adv. Mater. 2020, 32, 1907826.
- [18] Y. Cho, S. Pak, B. Li, B. Hou, S. Cha, Adv. Funct. Mater. 2021, 31, 2104239.
- [19] Y. Cho, S. Pak, B. Li, B. Hou, S. Cha, Nano Energy 2021, 81, 105626.
- [20] G. Pica, L. Pancini, C. E. Petoukhoff, B. Vishal, F. Toniolo, C. Ding, Y.-K. Jung, M. Prato, N. Mrkyvkova, P. Siffalovic, S. De Wolf, C.-Q. Ma, F. Laquai, A. Walsh, G. Grancini, *Nat. Commun.* 2024, *15*, 8753.
- [21] R. Korlacki, R. F. Saraf, S. Ducharme, Appl. Phys. Lett. 2011, 99, 153112.
- [22] D. Yang, J. Liang, J. Wu, Y. Xiao, J. I. Dadap, K. Watanabe, T. Taniguchi, Z. Ye, Nat. Commun. 2024, 15, 1389.
- [23] X. Qiu, S. Shen, X. Yue, S. Qin, C. Sheng, D. Xia, X. Huang, B. Tian, Y. Cai, Z.-J. Qiu, R. Liu, L. Hu, C. Cong, ACS Appl. Mater. Interfaces 2025, 17, 7027.
- [24] S. Plainis, I. J. Murray, W. N. Charman, Optom. Vis. Sci. 2005, 82, 682.
- [25] M. C. Kroes, G. Fernandez, Neurosci. Biobehav. Rev. 2012, 36, 1646.
- [26] A. E. Orhan, C. R. Sims, R. A. Jacobs, D. C. Knill, Curr. Dir. Psychol. Sci. 2014, 23, 164.
- [27] D. Gehrig, D. Scaramuzza, Nature 2024, 629, 1034.
- [28] R. E. Miller, T. J. Tredici, Night Vision Manual for the Flight Surgeon, Armstrong lab Brooks AFB, TX, USA, 1992.
- [29] A. Stockman, T. Candler, L. T. Sharpe, J. Vis. 2010, 10, 11.
- [30] J. Y. Kim, S. Lee, S. Lee, K. Lee, Y. Huh, Y. E. Kim, J. W. Lee, C. E. Lee, D. Kim, B.. Yim, J. Bang, Y. S. Cho, E. Kim, J. Huh, C. Park, J.-K. Lee, Cell Rep. Phys. Sci. 2022, 3, 101006.
- [31] Y. Huang, J. Tang, L. Gai, Y. Gong, H. Guan, R. He, H. Lyu, Chem. Eng. J. 2017, 319, 229.
- [32] M Machida, B Fotoohi, Y Amamo, T Ohba, H Kanoh, L Mercier, J. Hazard. Mater. 2012, 221-222, 220.
- [33] J Liu, H Du, S Yuan, W He, Z Liu, J. Environ. Chem. Eng. 2015, 3, 617.
- [34] S. K. Chacko, M. T. Rahul, B. Raneesh, N. Kalarikkal, New J. Chem. 2020, 44, 11356.
- [35] P. Martins, A. C. Lopes, S. Lanceros-Mendez, Prog. Polym. Sci. 2014, 39, 683
- [36] B. Jiang, X. Pang, B. Li, Z. Lin, J. Am. Chem. Soc. 2015, 137, 11760.
- [37] L. Gao, B.-L. Hu, L. Wang, J. Cao, R. He, F. Zhang, Z. Wang, W. Xue, H. Yang, R.-W. Li, *Science* 2023, 381, 540.

- [38] X. Li, S. Chen, P. F. Liu, Y. Zhang, Y. Chen, H. L. Wang, H. Yuan, S. Feng, J. Am. Chem. Soc. 2020, 142, 3316.
- [39] H. Pan, F. Li, Y. Liu, Q. Zhang, M. Wang, S. Lan, Y. Zheng, J. Ma, L. Gu, Y. Shen, P. Yu, S. Zhang, L.-Q. Chen, Y.-H. Lin, C.-W. Nan, *Science* 2019, 365, 578.
- [40] S. Han, T. Ma, H. Li, J. Wu, R. Liu, R. Cao, F. Li, H. Li, C. Chen, Adv. Funct. Mater. 2024, 34, 2309910.
- [41] K. Y. Lee, S. K. Kim, J.-H. Lee, D. Seol, M. K. Gupta, Y. Kim, S.-W. Kim, Adv. Mater. 2016, 26, 3067.
- [42] Y. Kim, C. Bae, K. Ryu, H. Ko, Y. K. Kim, S. Hong, H. Shin, Appl. Phys. Lett. 2009, 94, 032907.
- [43] Y. Kim, S. Buhlmann, J. Kim, M. Park, K. No, Y. K. Kim, S. Hong, Appl. Phys. Lett. 2007, 91, 052906.
- [44] D. Seol, G. S. Han, C. Bae, H. Shin, H. S. Jung, Y. Kim, J. Mater. Chem. A 2015, 3, 20352.
- [45] Y.-J. Kim, T.-V. Dang, H.-J. Choi, B.-J. Park, J.-H. Eom, H.-A. Song, D. Seol, Y. Kim, S.-H. Shin, J. Nah, S.-G. Yoon, J. Mater. Chem. A 2016, 4, 756.
- [46] S. Olthof, Adv. Opt. Mater. 2021, 9, 2100227.
- [47] H. Zhou, J. Park, Y. Lee, J.-M. Park, J.-H. Kim, J. S. Kim, H.-D. Lee, S. H. Jo, X. Cai, L. Li, X. Sheng, H. J. Yun, J.-W. Park, J.-Y. Sun, T.-W. Lee, Adv. Mater. 2020, 32, 2001989.
- [48] Y. Tian, M. Peter, E. Unger, M. Abdellah, K. Zheng, T. Pullerits, A. Yartsev, V. Sundström, I. G. Scheblykin, *Phys. Chem. Chem. Phys.* 2015, 17, 24978.
- [49] R. Brenes, C. Eames, V. Bulovic, M. S. Islam, S. D. Stranks, Adv. Mater. 2018, 30, 1706208.
- [50] H.-L. Park, H. Kim, D. Lim, H. Zhou, Y.-H. Kim, Y. Lee, S. Park, T.-W. Lee, Adv. Mater. 2020, 32, 1906899.
- [51] A. El Amrani, B. Lucas, F. Hijazi, A. Moliton, Mater. Sci. Eng. B 2008, 147, 303.
- [52] Y. Hu, G. Dong, L. Wang, Y. Qiu, Jpn. J. Appl. Phys. **2006**, 45, 196
- [53] H.-L. Park, Y. Lee, N. Kim, D.-G. Seo, G.-T. Go, T.-W. Lee, Adv. Mater. 2020, 32, 1903558.
- [54] R. Dallaev, T. Pisarenko, D. Sobola, F. Orudzhev, S. Ramazanov, T. Trčka, Polymers 2022, 14, 4793.
- [55] J. Lim, B. G. Jeong, M. Park, J. K. Kim, J. M. Pietryga, Y.-S. Park, V. I. Klimov, C. Lee, D. C. Lee, W. K. Bae, Adv. Mater. 2014, 26, 8034.
- [56] M. Lee, W. Lee, S. Choi, J. W. Jo, J. Kim, S. K. Park, Y.-H. Kim, Adv. Mater. 2017, 29, 1700951.